Analytic Modeling of Features in Attosecond Transient Absorption Spectrograms

Progress Report
Part A Qualifying Exam

Author: Jørgen Johansen Rørstad
Supervisor: Lars Bojer Madsen

April, 2017

Department of Physics and Technology
Aarhus University
Denmark

Preface

This progress report contains an overview of the work done during part A of my Ph.D. studies at the Department of Physics and Astronomy, Aarhus University. This work involves the derivation of analytical expressions representing several features which are commonly seen in the spectra of the method of attosecond transient absorption spectroscopy. The contents and structure of the progress report largely overlaps with a paper we submitted recently [1].

Units

Atomic units ($\hbar = e = m_e = a_0 = 1$) are used throughout this report, unless stated otherwise.

Acknowledgements

I would first like to thank my Ph.D. supervisor, Lars, who has given me great support; he is reliably helpful, patient and optimistic, regardless of the matter at hand. Thanks to Katérina for all her invaluable support throughout my Ph.D. I am grateful to the (past and present) members of my extended research group, QUSCOPE, for creating a nice work atmosphere. Finally, thanks to Jens E. Bækhøj for many fruitful discussions and successful collaboration.

Table of Contents

Chapter 1

Introduction

A hallmark of science is its unrelenting progression, which steadily unlocks new domains of research and exploration. In the field of atomic physics this is exemplified by the progress in laser technology which has enabled researchers to study some of the fastest processes in nature, ranging from the scale of femtoseconds (1 fs = 10^{-15} s) for atomic motion in molecules to attoseconds (1 as = 10^{-18} s) for bound electron dynamics. The control and measurement of processes occurring on these time scales are inherently dependent on the ability to produce pulses of equivalently short durations [2]. The attosecond threshold was only recently passed, with the creation of the first laser pulse with a sub-femtosecond duration shortly after the turn of the milennium [3]. Since then, researchers have been able to push the laser duration down to an incredible 67 as [4]. To offer some context, a beam of light traveling in vacuum would traverse a mere 20 nanometers in such a short period of time.

The production of extremely short laser pulses was facilitated by the discovery of high harmonic generation (HHG) [5, 6]. In HHG a target is exposed to an intense electric field, whereby electrons escape from the atoms or molecules, are accelerated in the field, recombine with the target, and emit photons with energies multiple times that of the photons in the incident field. This can be employed in a pump-probe setup where an initial infrared (IR) laser beam is split in two, with one part traveling directly to some atomic or molecular target, and the other part participating in the creation of an extreme utraviolet (XUV) pulse via HHG, after which the XUV pulse also proceeds to the target. Since the fields have the same origin, the delay between them can be very precisely controlled by varying the path length of the IR pulse.

Attosecond transient absorption spectroscopy (ATAS) is a fully optical method which makes use of the described pump-probe setup involving an XUV and an IR pulse. In ATAS, the spectrum of the XUV pulse is modified as it interacts with a target in conjunction with the IR dressing field. The electronic detector which captures the modified XUV spectrum operates at a time scale order of magnitudes slower than the processes happening in the target, and will only attain a time-integrated picture. Time is instead introduced in this method by the variable delay between the IR and XUV pulses, as described above. The full spectrograms obtained by this method display

absorption and emission, the interpretation of which can yield information about the processes undergone by the target atoms or molecules. The first experiment of this kind was performed by Goulielmakis et al [7], where they obtained time-resolved information about the attosecond motion of valence electrons in krypton. Since then the method has been widely used, for example in the study time-resolved autoionization in argon [8], and more recently in the real-time observation of an emerging Fano resonance [9].

The features found in ATA spectrograms, which correspond to physical processes, have been subject to theoretical scrutiny. These features include oscillating fringes, interpreted as signals of various forms of interference [10, 11]; light-induced structures (LISs) which indicate the presence of intermediate states in two-photon absorption processes [12]; hyperbolic sidebands (SBs) attributed to perturbed free-induction decay [13, 14]; and Autler-Townes splitting of the absorption lines, due to the resonant interaction between two states [15, 16, 17]. Here we restrict our focus to the features seen in Fig. 1.1, all of which typically are present in systems consisting of few levels and under the influence of moderately intense fields.

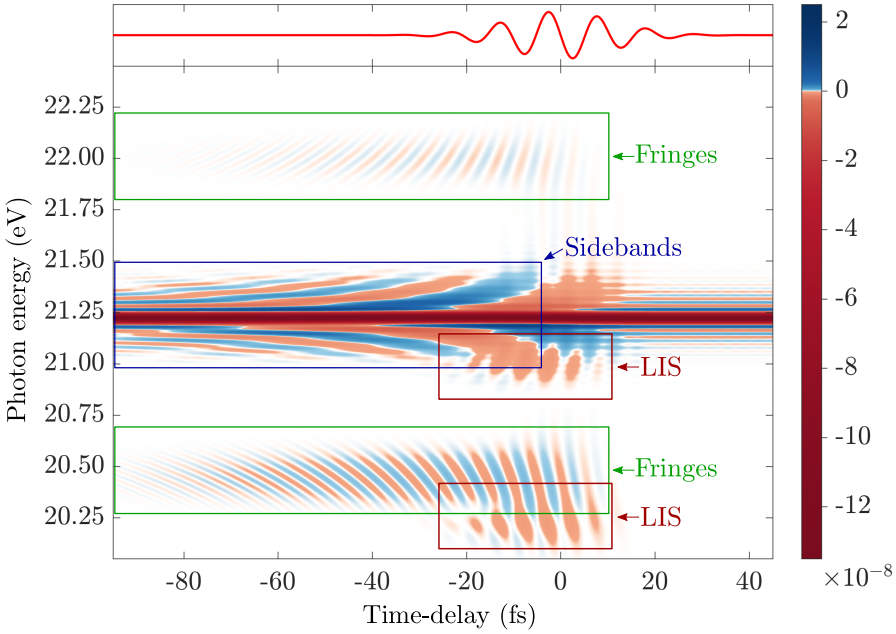

Figure 1.1: Attosecond transient absorption spectrum $\tilde{S}(\omega, \tau)$ [Eq. (2.1)] based on the adiabatic three-level model developed in Chapter 2, exemplified by He. Pertinent features are highlighted: Oscillating fringes centered around 22.00 eV and 20.45 eV; hyperbolic sidebands centered around 21.22 eV; and light-induced structures (LISs) centered around 21.01 eV and 20.23 eV. The top panel illustrates the infrared pulse centered at $\tau = 0$ fs. The color scale to the right shows the signal strength in arbitrary units. Analytical expressions will be derived for the highlighted features. For pulse parameters see text following Eq. (2.2).

In this progress report, we describe the derivation of closed analytical forms representing the interference fringes, LISs and SBs in atoms (see Fig. 1.1). The contents of

the report are in large part similar or identical to work detailed in a recently submitted manuscript [1] in which the main author was responsible for all calculations and the writing itself, with the support of the co-authors. The motivation behind obtaining analytical expressions describing these features is to enable a clearer understanding of their origin and their corresponding physical processes. Moreover, simple and accurate models may serve as a valuable aid in the extraction of attosecond dynamics directly from the ATA spectrum. The system the analytic derivation is based on contains three energy levels and is responding adiabatically to the IR field. A similar setup has been treated numerically by Dong et al [18], but an analytical treatment has been lacking. Given the proper field parameters, such a 3-level setup can correspond to three bound states in a number of systems, and in this work we use the three lowest levels of Helium as an example. To ensure that no information is lost in the energy range of interest when using only a small subset of the bound states in a system, we compare numerical solutions where we have included 3 and 20 energy levels.

The report is organized as follows. Chapter 2 introduces the theoretical framework of all relevant methods and models. Specifically, in Sec. 2.1 we show how to obtain the single-atom response function, which describes the modulation of the XUV field interacting with an IR field-dressed atom, and relevant information about the fields and parameters used in the work is given. In Sec. 2.2 we outline the process of numerically calculating the time-dependent dipole moment of an atom exposed to the fields mentioned above, utilizing the time-dependent Schrödinger equation (TDSE), and we examine the validity of the three-level ansatz of our model. Sec. 2.3 contains the derivation of the closed analytical forms corresponding to the features of interest, based on a three-level system subject to the adiabatic condition. In Chapter 3 we make comparisons between the various methods and the analytical expressions, followed by individual scrutiny of each of the three features of interest. Finally, Chapter 4 offers a summary and an outlook.

Chapter 2

Theory and discussion

The first section of this chapter introduces the response function of the system, from which we can obtain the delay-dependent ATA spectrum. In the next section, this response function is calculated for a system of bound states by a method involving numerical solutions of the TDSE. In the final section we derive analytic closed analytic forms corresponding to specific features of the ATA spectrum.

2.1 Single-atom response function

The intensities of the fields involved in the present work allows for a so-called semi-classical approach. In this approach the atomic systems are subject to a fully quantum mechanical treatment, whereas the fields are treated classically. This leads to a significant reduction in the complexity of the calculations. Here we use an XUV attosecond pulse, which excites the system at a given time $t = \tau$, along with a femtosecond IR pulse which induces a mixing (dressing) of the field free states. The pulse center of the IR pulse is fixed at $t = 0$, implying that the delay τ represents the relative position of the XUV pulse center. All fields are linearly polarized in the z-direction.

The delay-dependent single-atom response describes the modulation of the XUV field interacting with an IR field-dressed atom. This modulation is due to the interference between the incoming XUV pulse and the response of the time-dependent dipole moment of the target. Realistically a full description must include the medium of propagation, but for sufficiently dilute gases the single-atom response is a valid approximation [19]. The derivation of the response function is detailed in several works (see for example Ref. [20]), so we give the function here directly:

$$\tilde{S}(\omega, \tau) = \frac{4\pi n\omega}{c} \mathrm{Im}[\tilde{\mathcal{E}}^*_{\mathrm{in}}(\omega, \tau)\tilde{d}(\omega, \tau)]. \tag{2.1}$$

Here n is the density of atoms in the sample, $c \simeq 137$ is the speed of light, $\tilde{\mathcal{E}}_{\mathrm{in}}(\omega, \tau)$ is the incoming XUV field in the frequency domain and $\tilde{d}(\omega, \tau)$ is the expectation value of the dipole moment's z-component in the frequency domain. The tilde is used to denote Fourier transformed quantities, where the convention $\tilde{f}(\omega) = \frac{1}{\sqrt{2\pi}} \int_{-\infty}^{\infty} dt\, f(t) e^{-i\omega t}$ has

been used. In Eq. (2.1) a negative value corresponds to absorption, and a positive value corresponds to emission of light. There exists in the literature several expressions equivalent to the response function in Eq. (2.1), an overview and discussion of these can be found in Ref. [21].

All fields in this report are obtained from $\mathcal{E}(t) = -\partial_t A(t)$, where $A(t)$ is the vector potential given by

$$A(t) = A_0 \exp\left[-\frac{(t-t_c)^2}{T^2/4}\right] \cos\left[\omega(t-t_c)\right], \tag{2.2}$$

with $A_0 = \mathcal{E}_0/\omega$, and ω the angular frequency. $\mathcal{E}_0$ is related to the intensity by $I \propto |\mathcal{E}_0|^2$. In Eq. (2.2) t_c represents the center of the pulse, and the period is $T = N_c T_c = N_c \frac{2\pi}{\omega}$, where N_c is the number of cycles in the pulse and T_c is the period of one cycle. The period T is connected with the temporal full width at half maximum (FWHM) of the field through $T_{\mathrm{FWHM}} = \sqrt{\log 2}T$. For the IR pulse $t_c = 0$, and for the XUV pulse $t_c = \tau$. The specific pulse parameters used herein are as follows: $\lambda_{\mathrm{IR}} = 3200$ nm, $\lambda_{\mathrm{XUV}} = 50$ nm, $I_{\mathrm{IR}} = 6 \times 10^{10}$ W/cm^2, $I_{\mathrm{XUV}} = 5 \times 10^7$ W/cm^2, $T_{\mathrm{IR}} = 32.02$ fs ($N_{c,\mathrm{IR}} = 3$) and $T_{\mathrm{XUV}} = 330$ as ($N_{c,\mathrm{XUV}} = 2$). We arbitrarily set the density of atoms $n = 1$ [see Eq. (2.1)].

2.2 Time-dependent Schrödinger equation

The response function in Eq. (2.1) describes how the XUV field is modulated through the interaction with a dressed atomic system, which is what we seek to obtain through the method of ATAS. In order to do this, we calculate the expectation value of the time-dependent dipole moment $\langle d(t)\rangle \equiv \langle\Psi(t)|d|\Psi(t)\rangle$, with $d = -\sum_k z_k$ the dipole moment operator in the polarization direction. The quantum state of a system consisting solely of bound states can be expressed as

$$|\Psi(t)\rangle = \sum_{n=0}^{N} c_n(t) e^{-iE_n t} |\varphi_n\rangle \,, \tag{2.3}$$

with $|\phi_n\rangle$ an energy eigenstate of the unperturbed system corresponding to energy E_n and N the number of bound states in the finite basis of field free states. The omission of continuum states is a valid approximation under the present conditions [11]. The full Hamiltonian of the system is $H = H_0 + H'(t)$, where the time-dependent part accounts for the electric fields. Even with the small spatial extent of an attosecond pulse, the dipole approximation is still valid. With this approximation, and in the length gauge representation, the time-dependent part of the Hamiltonian is

$$H'(t) = -\mathcal{E}(t)d, \tag{2.4}$$

with $\mathcal{E}(t)$ the total field, including both the XUV and IR field. By inserting the quantum state from Eq. (2.3) into the TDSE and projecting on $\langle\phi_m|$ we obtain a set of coupled

differential equations for the coefficients $c_m(t)$

$$\frac{dc_m}{dt} = -i\mathcal{E}(t)\sum_{n=0}^{N} c_n(t)d_{mn}e^{i(E_m-E_n)t}, \tag{2.5}$$

with $d_{mn} = \langle\phi_m|d|\phi_n\rangle$ the transition dipole moment between states m and n. The solutions of Eqs. (2.5) are obtained numerically, and the time-dependent dipole moment is determined by

$$\langle\Psi(t)|d|\Psi(t)\rangle = \sum_{m,n=0}^{N} c_m^*(t)c_n(t)e^{-i(E_n-E_m)t}d_{mn}. \tag{2.6}$$

We use He to illustrate our theory, with energies and transition dipole moments given in Ref. [22].

In experiments, the time-dependent dipole moment will naturally undergo dephasing due to various effects, including collisional broadening and finite detector resolution. These effects must be artificially introduced in the present theory, and is achieved by imposing a window function $W(t-\tau)$ on the dipole moment in Eq. (2.6) [21, 23]. This window function dampens $\langle d(t)\rangle$ over an appropriate time T_0, starting at the moment when the XUV pulse arrives at the target. The time T_0 is chosen to be large enough that the features of interest in the ATA spectrum remain unaffected, which for the parameters used in this work is $T_0 = 120$ fs. The window function is defined as

$$W(t-\tau) = \begin{cases} 1 & (t < \tau) \\ \cos^2\left[\dfrac{(t-\tau)\pi}{2T_0}\right] & (\tau \le t \le \tau + T_0) \\ 0 & (t > \tau + T_0). \end{cases} \tag{2.7}$$

Multiplying Eq. (2.6) by the window function and taking the Fourier transform returns $\tilde{d}(\omega,\tau)$; the response function can then be determined from Eq. (2.1).

The method from this section serves as a reference to which we can compare our analytic model, which consists of three energy levels. To ensure a valid reference, we also require the TDSE calculations to be accurate for a three-level system [Eq. (2.3) with $N+1=3$]. By comparing solutions based on $N+1=20$ and $N+1=3$ bound states of the present model system, He, and confirming that they agree in the relevant range of energies, we verify that the exclusion of additional bound states in the excited state manifold does not affect the features of interest. A comparison of the two cases is shown in Fig. 2.1, where we have used the pulse parameters given in the text following Eq. (2.2) and the window function from Eq. (2.7). The energy range for which we require agreement between the two solutions extends from $\sim$ 20 eV to $\sim$ 22.4 eV. The only disparity is seen around 22.3 eV, where there is a change as we go from 20 levels in Fig. 2.1 (a) to 3 levels in Fig. 2.1 (b). In this region, oscillating fringes associated with the $|1s3p\rangle$ state is overlapping with the equivalent feature corresponding to the $|1s2p\rangle$ state. As the $|1s3p\rangle$ state is removed from the calculations, its corresponding fringes vanish and uncover the fringes associated with the $|1s2p\rangle$ state. Consequently, the three-level TDSE calculations can be considered accurate in the energy range of interest.

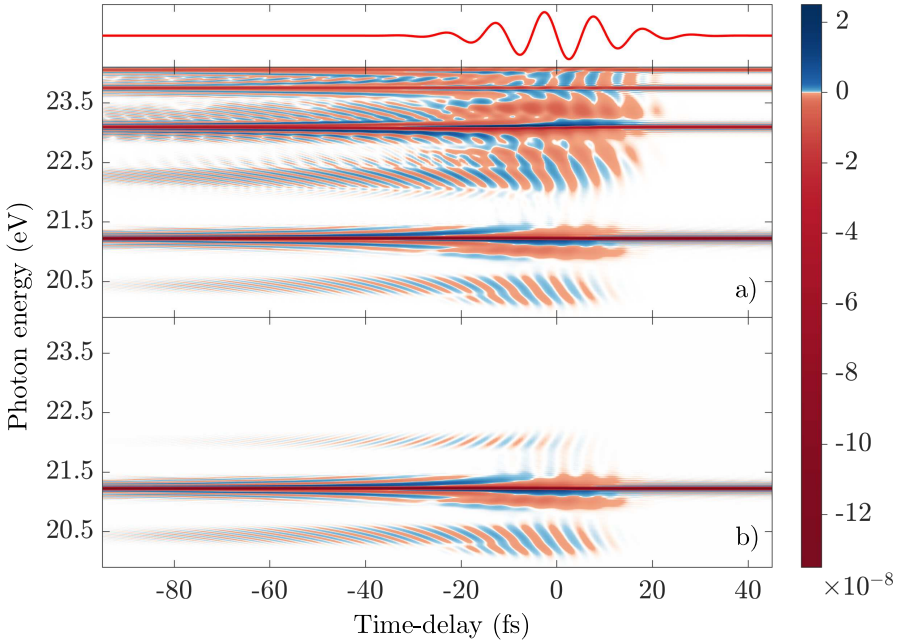

Figure 2.1: Attosecond transient absorption spectra $\tilde{S}(\omega, \tau)$ of He calculated by Eq. (2.1), where $\tilde{d}(\omega, \tau)$ is determined via the TDSE [see Eq. (2.6)]. In (a) the results are obtained with a basis consisting of the $N + 1 = 20$ lowest levels of He. In (b) the results are obtained with a basis consisting of only the $N + 1 = 3$ lowest levels of He; the ground state, fixed at 0 eV, $|1s2s\rangle$ at 20.62 eV, and $|1s2p\rangle$ at 21.22 eV. The top panel illustrates the infrared pulse centered at $\tau = 0$ fs. The color scale to the right shows the signal strength in arbitrary units. For pulse parameters see text following Eq. (2.2).

2.3 Adiabatic three-level model

In this section we obtain closed analytical expressions corresponding to features in the ATA spectrum, based on a system with three energy levels. To derive these expressions from Eq. (2.1), we start by determining the time-dependent dipole moment of the system, $\langle \Psi(t)|d|\Psi(t)\rangle$. After this, we apply perturbation theory and a number of approximations, which sequentially simplifies the expressions to the point where an analytical Fourier transform is attainable.

The starting ansatz is a three-level setup where only one of the excited states, designated as the bright state, is accessible through a dipole allowed transition from the ground state. For the other excited state, designated as the dark state, there exists no dipole allowed coupling with the ground state. These excited energy levels lie within the broad spectrum of frequencies in the XUV pulse. The IR pulse consists of low-frequency components and is too weak to excite the system via multiphoton absorption. The IR pulse will, however, induce a mixing of the excited states. This mixture of field-free states serves as a basis through which the adiabatic states can be expressed. We exemplify our model by the three lowest levels of He, where the bright state is $|1s2p\rangle$ and the dark

state is $|1s2s\rangle$.

For a system evolving adiabatically or near-adiabatically, an expansion in the adiabatic states $|\phi_{na}(t)\rangle$ defined through

$$H(t)\,|\phi_{na}(t)\rangle = E_{na}(t)\,|\phi_{na}(t)\rangle\,, \tag{2.8}$$

can be desirable. This equation expresses that the adiabatic states $|\phi_{na}(t)\rangle$ are the instantaneous eigenstates of $H(t)$, with eigenenergies $E_{na}(t)$. The solution to the TDSE can in the adiabatic basis be expressed as

$$|\Phi(t)\rangle = b_0(t)\,|\phi_0\rangle + a_1(t)\,|\phi_{1a}(t)\rangle\, e^{-i\int_\tau^t dt' E_{1a}(t')} + a_2(t)\,|\phi_{2a}(t)\rangle\, e^{-i\int_\tau^t dt' E_{2a}(t')}, \tag{2.9}$$

with the ground state energy E_0 set to zero, and $a_1(t)$, $a_2(t)$ the coefficients of the adiabatic states. The XUV field used in our calculations is weak, and consequently $a_1(t)$ and $a_2(t)$ will be small at all times. In Eq. (2.9) we have made the assumption that the ground state does not change appreciably under the influence of the fields, and denoted its coefficient by $b_0(t)$. $e^{-i\int_\tau^t dt' E_{na}(t')}$ $(n = 1, 2)$ is the phase factor for the adiabatic states with time-dependent energies.

We wish to obtain expressions for the adiabatic states and their associated energies. We start by considering the full Hamiltonian of our system

$$\underline{\underline{H_f}} = \begin{bmatrix} 0 & d_{01}\mathcal{E}_{\mathrm{XUV}}(t) & 0 \\ d_{01}\mathcal{E}_{\mathrm{XUV}}(t) & E_1 & d_{12}\mathcal{E}_{\mathrm{IR}}(t) \\ 0 & d_{12}\mathcal{E}_{\mathrm{IR}}(t) & E_2 \end{bmatrix}, \tag{2.10}$$

which illustrates the coupling, due to the XUV pulse, between the ground state and the first excited state; and similarly for the two excited states, coupled by the IR pulse. We have chosen the coupling such that $|\phi_1\rangle$ is the bright state and $|\phi_2\rangle$ is the dark state with respect to a dipole transition from the field-free ground state $|\phi_0\rangle$.

The Hamiltonian of Eq. (2.10) can be reduced by noting that after the XUV pulse has populated the first excited state, the ground state is approximately fixed and we effectively have a two-level system specified by

$$\underline{\underline{H}} = \begin{bmatrix} E_1 & d_{12}\mathcal{E}_{\mathrm{IR}}(t) \\ d_{12}\mathcal{E}_{\mathrm{IR}}(t) & E_2 \end{bmatrix}. \tag{2.11}$$

From this Hamiltonian we can obtain the instantaneous eigenvalues

$$E_{1a}(t) \approx E_1 + \frac{d_{12}^2\mathcal{E}_{\mathrm{IR}}^2(t)}{E_1 - E_2}, \tag{2.12}$$

$$E_{2a}(t) \approx E_2 - \frac{d_{12}^2\mathcal{E}_{\mathrm{IR}}^2(t)}{E_1 - E_2}. \tag{2.13}$$

In obtaining Eqs. (2.12) and (2.13) we have performed a Taylor expansion about $\mathcal{E}_{\mathrm{IR}}(t) = 0$ and neglected terms of third order or higher in the IR field. The normalized adiabatic eigenstates are

$$|\phi_{1a}(t)\rangle = \frac{d_{12}\mathcal{E}_{\mathrm{IR}}(t)}{\sqrt{d_{12}^2\mathcal{E}_{\mathrm{IR}}^2(t) + [E_{1a}(t) - E_1]^2}}\,|\phi_1\rangle + \frac{E_{1a}(t) - E_1}{\sqrt{d_{12}^2\mathcal{E}_{\mathrm{IR}}^2(t) + [E_{1a}(t) - E_1]^2}}\,|\phi_2\rangle \tag{2.14}$$

and

$$|\phi_{2a}(t)\rangle = \frac{E_{2a}(t) - E_2}{\sqrt{d_{12}^2 \mathcal{E}_{\rm IR}^2(t) + [E_{2a}(t) - E_2]^2}} |\phi_1\rangle + \frac{d_{12}\mathcal{E}_{\rm IR}(t)}{\sqrt{d_{12}^2 \mathcal{E}_{\rm IR}^2(t) + [E_{2a}(t) - E_2]^2}} |\phi_2\rangle \,, \tag{2.15}$$

which appropriately reduce to the field-free states in the limit $\mathcal{E}_{\rm IR}(t) \to 0$.

The next step is to determine the coefficients $a_1(t)$ and $a_2(t)$ of Eq. (2.9). It is convenient to first express the quantum state in terms of field-free basis states:

$$|\Phi(t)\rangle = b_0(t)\,|\phi_0\rangle + b_1(t)\,|\phi_1\rangle + b_2(t)\,|\phi_2\rangle \,, \tag{2.16}$$

where the coefficients are

$$b_1(t) = a_1(t) e^{-i\int_\tau^t dt' E_{1a}(t')} \langle \phi_1 | \phi_{1a}(t)\rangle + a_2(t) e^{-i\int_\tau^t dt' E_{2a}(t')} \langle \phi_1 | \phi_{2a}(t)\rangle \,, \tag{2.17}$$

and

$$b_2(t) = a_1(t) e^{-i\int_\tau^t \mathrm{d}t' E_{1a}(t')} \langle \phi_2 | \phi_{1a}(t)\rangle + a_2(t) e^{-i\int_\tau^t \mathrm{d}t' E_{2a}(t')} \langle \phi_2 | \phi_{2a}(t)\rangle \,. \tag{2.18}$$

The overlaps $\langle \phi_m | \phi_{na}(t)\rangle$ $(n, m = 1, 2)$ can be obtained from Eqs. (2.14) and (2.15):

$$\langle \phi_1 | \phi_{1a}(t)\rangle = \langle \phi_2 | \phi_{2a}(t)\rangle \approx 1 - \frac{d_{12}^2 \mathcal{E}_{\rm IR}^2(t)}{2(E_1 - E_2)^2}, \tag{2.19}$$

$$\langle \phi_1 | \phi_{2a}(t)\rangle = -\langle \phi_2 | \phi_{1a}(t)\rangle \approx -\frac{d_{12}\mathcal{E}_{\rm IR}(t)}{E_1 - E_2}, \tag{2.20}$$

where we have neglected terms of third order or higher in the IR field after an expansion about $\mathcal{E}_{\rm IR}(t) = 0$.

We insert Eq. (2.16) into the TDSE and project onto each of the excited field-free states, $|\phi_1\rangle$ and $|\phi_2\rangle$, thus obtaining equations for the coefficients $\dot{a}_1(t)$ and $\dot{a}_2(t)$ (dot denotes time-derivative). These coefficients are then treated perturbatively. In the zeroth order approximation the system stays unperturbed, and we expect it to remain in the ground state indefinitely, i.e. $b_0^{(0)}(t) = 1$, $a_1^{(0)}(t) = a_2^{(0)}(t) = 0$ (superscripts denote the order of approximation). To obtain the first order approximations for the coefficients, we insert the zeroth order coefficients back into our differential equations. Neglecting third order or higher terms of IR field in the pre-exponential factor, the equations become

$$\dot{a}_1^{(1)}(t) \approx i d_{01} \mathcal{E}_{\rm XUV}(t) e^{i\int_\tau^t dt' E_{1a}(t')}, \tag{2.21}$$

$$\dot{a}_2^{(1)}(t) \approx -\frac{i d_{01} d_{12}}{E_1 - E_2} \mathcal{E}_{\rm XUV}(t) \mathcal{E}_{\rm IR}(t) e^{i\int_\tau^t dt' E_{2a}(t')}. \tag{2.22}$$

The change in the coefficient of the ground state is assumed to be negligible throughout the interaction, and so we have set $b_0(t) = 1$.

From this point on it is practical to work directly with the expectation value of the time-dependent dipole moment. To leading order in the small coefficients $b_1(t)$ and $b_2(t)$, we obtain

$$\langle \Phi(t) | d | \Phi(t)\rangle = \langle d(t)\rangle = d_{01}\left[b_1(t) + b_1^*(t)\right], \tag{2.23}$$

where we have used that $d_{02} = 0$. The $b_1(t)$ coefficient contains factors $e^{-iE_1 t}$ and $e^{-iE_2 t}$, which upon Fourier transform correspond to shifts to negative frequencies. Since we need only consider positive frequency, we keep only $b_1^*(t)$, yielding

$$\langle d(t)\rangle = d_{01}\left[a_1^*(t)e^{i\int_\tau^t dt' E_{1a}(t')}\langle\phi_1|\phi_{1a}(t)\rangle^* + a_2^*(t)e^{i\int_\tau^t dt' E_{2a}(t')}\langle\phi_1|\phi_{2a}(t)\rangle^*\right], \quad (2.24)$$

which is multiplied by the window function $W(t-\tau)$ [see Eq. (2.7)] to account for dephasing.

We now have a complete model of the three-level system. By numerically solving Eqs. (2.21) and (2.22) and inserting the solution into Eq. (2.24) we obtain the time-dependent dipole moment. This is then numerically Fourier transformed and inserted into Eq. (2.1), along with the Fourier transform of the XUV pulse, yielding the response function of the system.

To further progress toward an analytical form of the response function, we perform a series of approximations. The first is to assume that the XUV pulse is sufficiently brief that its time-dependence can be approximated by the Dirac delta function [23]

$$\mathcal{E}_{\mathrm{XUV}}(t) \to \alpha\delta(t-\tau), \quad (2.25)$$

with α a constant in a given set of field parameters, its value determined by comparison with an equivalent numerical solution for the response function. In the present calculations we have $\alpha = 1.61 \times 10^{-4}$. With integrands containing delta functions, the integration of Eqs. (2.21) and (2.22) is trivial:

$$a_1^{(1)}(t) = \int_\tau^t dt' \dot{a}_1^{(1)}(t') = i\alpha d_{01}\theta(t-\tau) \quad (2.26)$$

$$a_2^{(1)}(t) = \int_\tau^t dt' \dot{a}_2^{(1)}(t') = -\frac{i\alpha d_{01} d_{12}}{E_1 - E_2}\theta(t-\tau)\mathcal{E}_{\mathrm{IR}}(\tau), \quad (2.27)$$

where $\theta(t-\tau)$ is the Heaviside step function. As will be shown later, the two terms in Eq. (2.24) correspond to distinct features in the ATA spectrum. The first gives rise to delay-dependent SBs [11, 10] and oscillating fringes [11] associated with the E_1 energy level; the second generates LISs [12] associated with the E_2 energy level (see Fig. 3.1). In the following subsections, we treat the terms separately.

2.3.1 Closed analytical form of SBs and oscillating fringes and discussion of physical origins

From the first term in Eq. (2.24) we have [see Eq. (2.26)]

$$\langle d(t)\rangle_1 = -i\alpha d_{01}^2\theta(t-\tau)e^{i\int_\tau^t dt' E_{1a}(t')}\langle\phi_1|\phi_{1a}(t)\rangle^*. \quad (2.28)$$

From Eq. (2.12) we see that the exponential factor in Eq. (2.28) can be separated as $\exp\left[i\int_\tau^t dt' E_{1a}(t')\right] = \exp\left[iE_1(t-\tau)\right]\exp\left[id_{12}^2(E_1-E_2)^{-1}\int_\tau^t dt'\mathcal{E}_{\mathrm{IR}}^2(t')\right]$. We expand the exponential factor to first order, which is accurate because $\mathcal{E}_{\mathrm{IR}}^2(t)$ is small

$$e^{\frac{id_{12}^2}{E_1-E_2}\int_\tau^t dt'\mathcal{E}_{\mathrm{IR}}^2(t')} \approx 1 + \frac{id_{12}^2}{E_1-E_2}\int_\tau^t dt'\mathcal{E}_{\mathrm{IR}}^2(t'). \quad (2.29)$$

We then obtain [see Eq. (2.19)]:

$$\langle d(t)\rangle_1 = -i\alpha d_{01}^2\theta(t-\tau)e^{iE_1(t-\tau)}\left[1-\frac{d_{12}^2\mathcal{E}_{\rm IR}^2(t)}{2(E_1-E_2)^2}+\frac{id_{12}^2}{E_1-E_2}\int_\tau^t dt'\mathcal{E}_{\rm IR}^2(t')+O(\mathcal{E}_{0,\rm IR}^4)\right], \tag{2.30}$$

where the term of fourth order in the IR field can be neglected.

The features of the ATA spectrum that we are concerned with in the present study arise from temporary changes in the time-dependent dipole moment due to the influence of the IR field on the excited states. The Heaviside function $\theta(t-\tau)$ and the window function $W(t-\tau)$ impose restrictions on infinite oscillations that otherwise would correspond to discrete values in the frequency domain. We proceed by setting $\theta(t-\tau)=1$, excluding $W(t-\tau)$, and dropping the term from Eq. (2.30) whose only time-dependence is in the factor e^{iE_1t}:

$$\langle d(t)\rangle_1 = \frac{\alpha d_{01}^2 d_{12}^2}{E_1-E_2}e^{-iE_1\tau}e^{iE_1t}\left[\int_\tau^t dt'\mathcal{E}_{\rm IR}^2(t')+\frac{i\mathcal{E}_{\rm IR}^2(t)}{2(E_1-E_2)}\right]. \tag{2.31}$$

The consequence of neglecting $W(t-\tau)$ and $\theta(t-\tau)$ is a nonzero population in the excited states at all times. Before this approximation the IR pulse could not influence the system prior to the arrival of the XUV pulse, so beyond relatively small positive delays τ the ATA spectrum would simply exhibit a single photon absorption pattern; whereas for relatively large negative τ the system would have time to dephase prior to the arrival of the IR pulse (see Fig. 2.1). After this approximation the ATA spectrum is symmetric about $\tau=0$, and does not weaken at large negative τ. Moreover, as the term which only depends on time in the factor e^{iE_1t} is dropped, the main absorption line at $E=E_1$ corresponding to single photon absorption vanishes. We set out to explain analytically only the features highlighted in Fig. 1.1, so this disappearance does not pose a problem.

The Fourier transformed time-dependent dipole moment $\tilde{d}_1(\omega,\tau)$ can now be obtained from Eq. (2.31) (see the Appendix for details). The Fourier transform of the XUV field is simply $\tilde{\mathcal{E}}_{\rm XUV}(\omega,\tau)=\frac{\alpha}{\sqrt{2\pi}}e^{-i\omega\tau}$. Insertion into Eq. (2.1) yields the following expression for the response function

$$\begin{aligned}\tilde{S}_1(\omega,\tau) =& \frac{\sqrt{\pi}\alpha^2 d_{01}^2 d_{12}^2\mathcal{E}_{0,\rm IR}^2 T_{\rm IR} n}{4\sqrt{2}(E_1-E_2)c}\omega\cos\left[\tau(E_1-\omega)\right]\left[\frac{1}{\omega-E_1}-\frac{1}{2(E_1-E_2)}\right]\\ &\times\left\{\exp\left[\frac{-T_{\rm IR}^2(\omega-E_1+2\omega_{\rm IR})^2}{32}\right]+\exp\left[\frac{-T_{\rm IR}^2(\omega-E_1-2\omega_{\rm IR})^2}{32}\right]\right.\\ &\left.-2\exp\left[\frac{-T_{\rm IR}^2(\omega-E_1)^2}{32}\right]\right\}.\end{aligned} \tag{2.32}$$

The divergence at $\omega=E_1$ can be removed by assigning a finite radiative lifetime, Γ, to the E_1 level by the substitution $E_1\to E_1-i\Gamma/2$.

The SBs and fringes are described by Eq. (2.32), and from it we can identify the origin of these features. From Eqs. (2.28)-(2.31) we see that there are two interfering sources; one originates in the field-induced time-dependence of the adiabatic phases $e^{i\int_\tau^t E_{1a}(t)}$

and leads to the $1/(\omega - E_1)$ term; the other originates in the term related to the mixing of states, the complex conjugated overlap $\langle\phi_1|\phi_{1a}(t)\rangle^*$ between the first field-free state and the first adiabatic state, and gives rise to the constant term $-1/[2(E_1 - E_2)]$. These two terms interfere constructively for $\omega < E_1$ and destructively for $\omega > E_1$, resulting in the asymmetry in the signal strength of the fringes (see Fig. 3.3). The exponentials in Eq. (2.32) cause Gaussian modulation about the energies $\omega = E_1$ (SBs) and $\omega = E_1 \pm 2\omega_{\mathrm{IR}}$ (fringes). They emerge in the Fourier transform of the squared IR field [see Eqs. (A.9) and (A.10)], and we note specifically that the $\exp\left[-T_{\mathrm{IR}}^2(\omega - E_1 \pm 2\omega_{\mathrm{IR}})/32\right]$ terms are due to the carrier factor $\sin(\omega_{\mathrm{IR}}t)$ of the IR field. The implication is that in the presence of an IR field consisting only of an envelope part the fringes would be absent, but the SBs would be present. The hyperbolic shape of the SBs and the oscillation of the fringes are both manifestations of the same factor, $\cos[\tau(\omega - E_1)]$, causing the features to follow hyperbolic trajectories where $\tau(\omega - E_1) = \text{constant}$ [23]. Thus the present formalism presents a unified description of the SBs and the fringes, two ATAS features previously attributed to separate processes, namely perturbed free-induction decay [13, 14] and optical interference [11]. The cosine term comes from the τ-dependent part of the phase-factor, $e^{-iE_1\tau}$, combined with the $e^{-i\omega\tau}$ factor of the XUV field. Finally, we recall that Eq. (2.32), and by extension the SBs and fringes, came from the first term in Eq. (2.24), which is associated with the first adiabatic states, which in turn was borne out of the field-free $|1s2p\rangle$ bright state.

2.3.2 Closed analytical form of LISs and discussion of physical origins

We return to Eq. (2.24) and consider now the second term. We expand the exponential factor in orders of the IR field, insert the overlap from Eq. (2.20), and drop terms of third order or higher in the IR field. Following the same reasoning as in Sec. 2.3.1, we exclude $W(t - \tau)$ and set $\theta(t - \tau) = 1$, yielding

$$\langle d(t)\rangle_2 = -\frac{i\alpha d_{01}^2 d_{12}^2}{(E_1 - E_2)^2}\mathcal{E}_{\mathrm{IR}}(\tau)e^{-iE_2\tau}e^{iE_2t}\mathcal{E}_{\mathrm{IR}}(t), \tag{2.33}$$

from which we can obtain the frequency-dependent dipole moment (see the Appendix for details). The response function is

$$\begin{aligned}\tilde{S}_2(\omega,\tau) =& \frac{\sqrt{\pi}\alpha^2 d_{01}^2 d_{12}^2 \mathcal{E}_{0,\mathrm{IR}}^2 T_{\mathrm{IR}} n}{2\sqrt{2}(E_1 - E_2)^2 c}\omega \exp\left(\frac{-4\tau^2}{T_{\mathrm{IR}}^2}\right)\sin(\omega_{\mathrm{IR}}\tau)\sin[\tau(E_2 - \omega)] \\ &\times\left\{\exp\left[-\frac{T_{\mathrm{IR}}^2(\omega - E_2 - \omega_{\mathrm{IR}})^2}{16}\right] - \exp\left[-\frac{T_{\mathrm{IR}}^2(\omega - E_2 + \omega_{\mathrm{IR}})^2}{16}\right]\right\}.\end{aligned} \tag{2.34}$$

Equation (2.34) describes the LISs, implying that their origin can be deduced from it. Unlike the case for the SBs and fringes [see Eq. (2.32)], the LISs cannot be ascribed to the adiabatic phases. They are instead a result of the complex conjugated coefficient $a_2^*(t)$ corresponding to the adiabatic $|\phi_{2a}(t)\rangle$ state, and the complex conjugate of its overlap with the first field-free state, $\langle\phi_1|\phi_{2a}(t)\rangle$ [see Eq. (2.24)]. Considering first the coefficient $a_2(t)$, from Eqs. (2.22) we see clearly the two-photon character of the process

responsible for the LISs, in agreement with previous interpretations [12]. Since the XUV field is approximated by a constant times a delta function [see Eqs. (2.25) and (2.27)] the subsequent integration 'picks out' the instantaneous value of the IR field at the time τ. This implies that the signal strength of the LIS will follow the IR field, and vanish when the field goes to zero (see Fig. 3.4); this behaviour is described by the $\exp\left[-4\tau^2/T_{\mathrm{IR}}^2\right]\sin\left[\omega_{\mathrm{IR}}\tau\right]$ part of Eq. (2.34). The overlap $\langle\phi_1|\phi_{2a}(t)\rangle^*$ is linear in the IR field, which upon Fourier transform leads to the terms $\exp\left[-T_{\mathrm{IR}}^2(\omega - E_2 \pm \omega_{\mathrm{IR}})^2/16\right]$ that cause Gaussian modulation of the features about energies $E_2 \pm \omega_{\mathrm{IR}}$. Furthermore, the delay dependent part of the phase, $e^{-iE_2\tau}$, combines with the $e^{-i\omega\tau}$ factor of the XUV field to produce the $\sin\left[\tau(E_2 - \omega)\right]$ factor, causing the LISs to take on hyperbolic shapes, like the SBs and fringes. We note finally that the LISs originate in the second term of Eq. (2.24), corresponding to the second adiabatic state, which in turn evolved from the field-free $|1s2s\rangle$ dark state.

Chapter 3

Results and comparisons

In this chapter the results obtained from the models described in Chapter 2 are presented. A comparison between the three-level TDSE solution and the full adiabatic three-level model is shown, and the features of main interest in the present work are highlighted. The focus then shifts to the features individually; specifically how they each change as we go from the TDSE solution to the analytic solution via the full adiabatic model.

The parameters given in Chapter 2 following Eq. (2.2) are chosen so as to fulfill two criteria. The fields must have relatively weak intensities and the wavelength of the IR field must be chosen so that it is not in resonance with the bright state to dark state transition. The first condition is necessary for the validity of first-order perturbation theory out of the ground state [see Eqs. (2.21) and (2.22)], and the latter condition is necessary for an adiabatic treatment of the excited states. The relatively weak intensity of the IR pulse ensures that the expansions in orders of $\mathcal{E}_{\mathrm{IR}}(t)$ in Sec. 2.3 are accurate. Finally, the IR wavelength must be long enough not to induce significant coupling between the three lowest levels of He and the higher levels in the bound-state manifold, to justify the use of a model with only these three levels. All generic features of interest will still be present in ATA spectra subject to these conditions, and the findings therefore also apply to other atoms where similar states and couplings can be realized.

In Fig. 3.1, we compare the three-level TDSE results obtained from Sec. 2.2 [see Eq. (2.6) with $N+1=3$; Fig. 3.1 (a)], with the full adiabatic three-level model results obtained from Eqs. (2.12), (2.13), (2.19)-(2.22), (2.24) [Fig. 3.1 (b)], and highlight the specific features of the spectrum that are included in the present work (as in Fig. 1.1). These features will be treated in detail individually, but are briefly described here. The features labeled 'Sidebands' are the SBs along the main absorption band of the $|1s2p\rangle$ states, which are often attributed to perturbed free-induction decay [14, 13]. The figure shows that the SBs are very well reproduced by the adiabatic model. The features labeled 'Fringes' are oscillating with a frequency twice that of the IR field frequency, and are found centered at energies $E(1s2p) \pm 2\omega_{\mathrm{IR}}$. They are reproduced quite well in the adiabatic model; the main difference being a weakening of the fringes centered at $E(1s2p) + 2\omega_{\mathrm{IR}}$ relative to the TDSE calculations. Note that the fringes are not 'which-way' fringes, which require additional bound states [12], but rather the type of

fringes attributed to optical interference in Ref. [11]. Finally, the LISs appear only where there is temporal overlap between the XUV and IR field [12]. They are centered at energies $E(1s2s) \pm \omega_{\mathrm{IR}}$ and like the fringes they exhibit modulation at twice the IR frequency. There are differences between the TDSE and the adiabatic model calculations when it comes to the LISs, but characteristics such as oscillation frequency, strength and position of the features are reproduced.

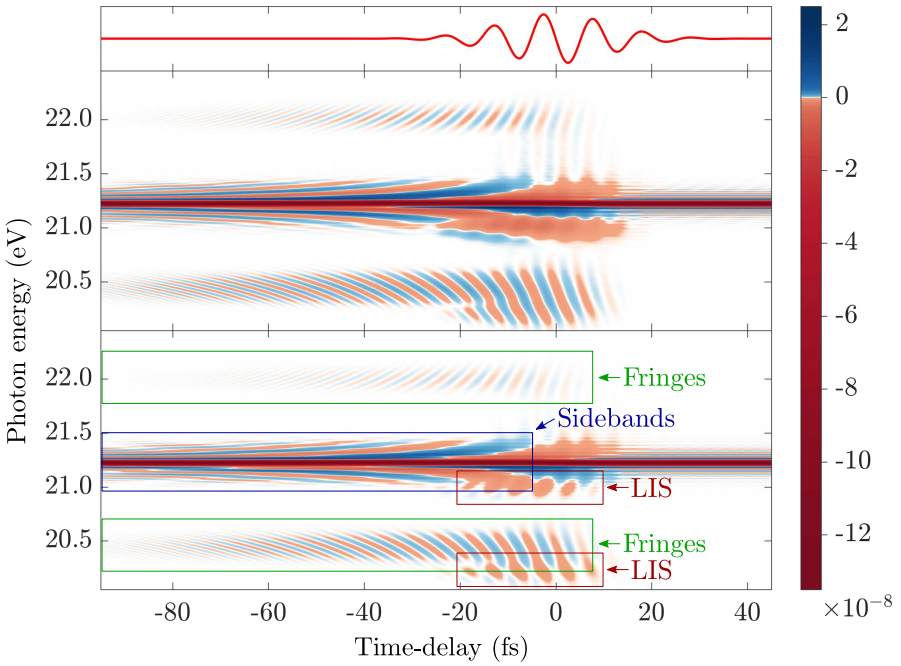

Figure 3.1: Attosecond transient absorption spectra $\tilde{S}(\omega, \tau)$ of He calculated by Eq. (2.1). In (a) $\tilde{d}(\omega, \tau)$ is determined via the time-dependent Schrödinger equation [see Eq. (2.6)] with a basis of $N + 1 = 3$ levels, as in Fig. 2.1 (b). In (b) $\tilde{d}(\omega, \tau)$ is calculated from the full adiabatic three-level model [see Eq. (2.24)] and several features of the spectrum are highlighted. Oscillating fringes are centered around $E(1s2p) \pm 2\omega_{\mathrm{IR}}$, i.e. at 22.00 eV and 20.45 eV; hyperbolic sidebands are centered around $E(1s2p) = 21.22$ eV; and light-induced structures (LISs) are centered around $E(1s2s) \pm \omega_{\mathrm{IR}}$, i.e. at 21.01 eV and 20.23 eV. The top panel illustrates the infrared pulse centered at $\tau = 0$ fs. The color scale to the right shows the signal strength in arbitrary units. For pulse parameters see text following Eq. (2.2).

The analytical expressions obtained in Sec. 2.3 contain the three different classes of features shown in Fig. 3.1. To support the validity of the expressions, we compare the features as they are calculated by the successive methods; first from the three-level TDSE, followed by the full adiabatic three-level model, and finally the analytical expressions.

3.1 Sidebands

The SBs as calculated by the various methods are shown in Fig. 3.2. The three-level TDSE solution can be seen in Fig. 3.2 (a). The adiabatic model calculations in Fig. 3.2 (b) are in good agreement with the TDSE results. The full adiabatic model [Eq. (2.24)] consists of two terms, only the second of which is responsible for the LISs. Since, for now, we are concerned with the SBs, this second term is dropped. The same simplification cannot be attained for the TDSE solution, as there is no equivalent single term accountable for the LISs in that method. This explains the presence of a LIS (centered at $E = 21.00$ eV and between $\tau = -25$ fs and $\tau = 15$ fs) in Fig. 3.2 (a), and its absence in Fig. 3.2 (b). In Fig. 3.2 (c) the analytical solution of Eq. (2.32) is shown, from which the term containing the $-2\exp\left[-T_{\mathrm{IR}}^2(\omega - E_1)^2/32\right]$ factor corresponds to the SBs. The SBs are well reproduced by the analytic expressions, both qualitatively and quantitatively. The differences between the analytical solution and the full adiabatic model can be attributed

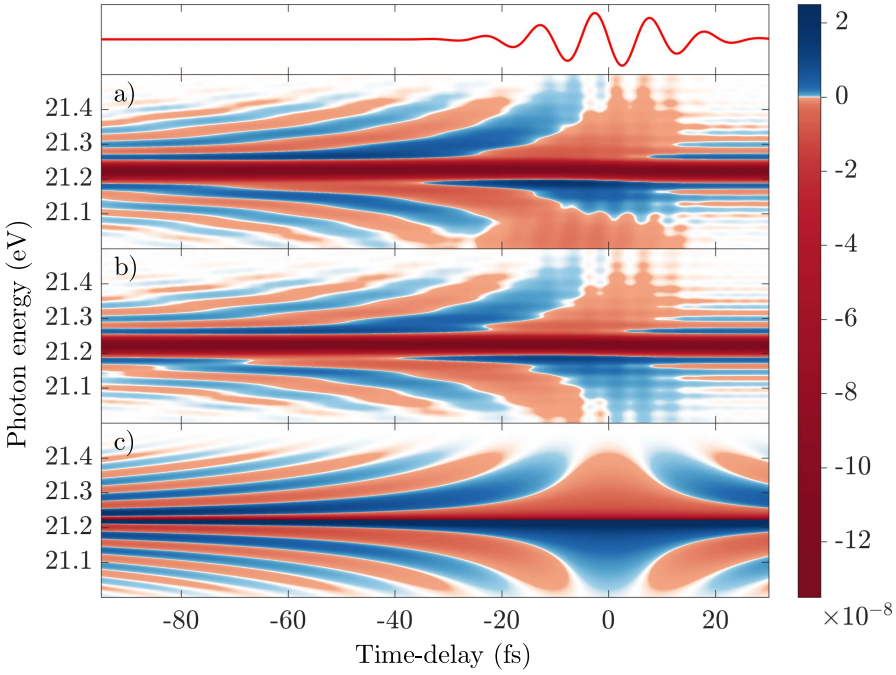

Figure 3.2: Attosecond transient absorption spectra $\tilde{S}(\omega, \tau)$ [Eq. (2.1)] focused on the hyperbolic sidebands (SBs) around the $|1s2p\rangle$ energy level of He. In (a) $\tilde{d}(\omega, \tau)$ is determined via the time-dependent Schrödinger equation [see Eq. (2.6)] with a basis of $N + 1 = 3$ levels, as in Fig. 2.1 (b). In (b) $\tilde{d}(\omega, \tau)$ is calculated from the adiabatic three-level model, with the light-induced structures seen in (a) (between -25 fs $< \tau <$ 15 fs, centered at $E = 21.00$ eV) removed by keeping only the first term of Eq. (2.24); resulting in an unobstructed view of the SBs. (c) shows the analytic solution from Eq. (2.32). The top panel illustrates the infrared pulse centered at $\tau = 0$ fs. The color scale to the right shows the signal strength in arbitrary units. For pulse parameters see text following Eq. (2.2).

to the removal of separate interfering features and the suppression of $W(t-\tau)$ and $\theta(t-\tau)$ as detailed in Sec. 2.3.1 leading up to Eq. (2.32).

3.2 Oscillating fringes

The oscillating fringes, as calculated by the various methods, are seen in Fig. 3.3. The panels above the dashed lines correspond to the fringes centered at the energy $E(1s2p) + 2\omega_{\mathrm{IR}} = 22.00$ eV and the panels below correspond to the fringes centered at $E(1s2p) - 2\omega_{\mathrm{IR}} = 20.45$ eV. The three-level TDSE solution can be seen in Fig. 3.3 (a), and as in Fig. 3.2 there is a LIS (centered at $E = 20.23$ eV, between -25 fs $< \tau < 15$ fs) which should not be considered part of the comparison. We note an asymmetry in the strength of the fringes, where the fringes at 22.00 eV are weaker; as understood from Eq. (2.32), this is due to interference between a term corresponding to the adiabatic phase and a term describing the mixing of the field-free states. In Fig. 3.3 (b) the results from the three-level adiabatic model are shown, and except from being slightly fainter they are in good qualitative and quantitative agreement with the TDSE results. The analytic solution from Eq. (2.32) is shown in Fig. 3.3 (c), where the contribution from the term containing the $\exp\left[-T_{\mathrm{IR}}^2(\omega - E_1 \pm 2\omega_{\mathrm{IR}})^2/32\right]$ factor produces the fringes. The fringes are reproduced with good qualitative and quantitative agreement; the main characteristics with which we are concerned are not affected by the differences between the analytic solution and the full adiabatic model. The causes of these differences are the same as for the SBs considered above, and are discussed in Sec. 2.3.1.

3.3 Light-induced structures

In Fig. 3.4 a comparison of the LISs calculated by the various methods is shown. The panels above the dashed lines correspond to the LISs centered at the energy $E(1s2s) + \omega_{\mathrm{IR}} = 21.01$ eV and the panels below correspond to the LISs centered at the energy $E(1s2s) - \omega_{\mathrm{IR}} = 20.23$ eV. The three-level TDSE solution is shown in Fig. 3.4 (a), where the LISs are seen along with the other features. As explained previously, the features cannot be distinguished and separated in the TDSE solutions, something which is possible in the adiabatic model. In the top panel of Fig. 3.4 (a) the LIS is mixed with the SBs and in the bottom panel the LIS is mixed with the lower oscillating fringes, somewhat complicating the comparison with the other calculations. The top LIS only takes on negative values, whereas the bottom LIS oscillates between positive and negative values similarly to the adjacent fringes. In the adiabatic model the LISs correspond to the second term of Eq. (2.24) and the other features correspond to the first term, so by keeping only the second term we can focus entirely on the LISs, the result of which is seen in Fig. 3.4 (b). There is significant departure from the TDSE-based calculations in Fig. 3.4 (a), but the key characteristics are still present. The features are confined to the same time-delays τ, the oscillation patterns match, and the strengths of the features are similar. The differences are likely attributable to the mentioned mixing of features in Fig. 3.4 (a) and the approximations made in the adiabatic model calculations. The

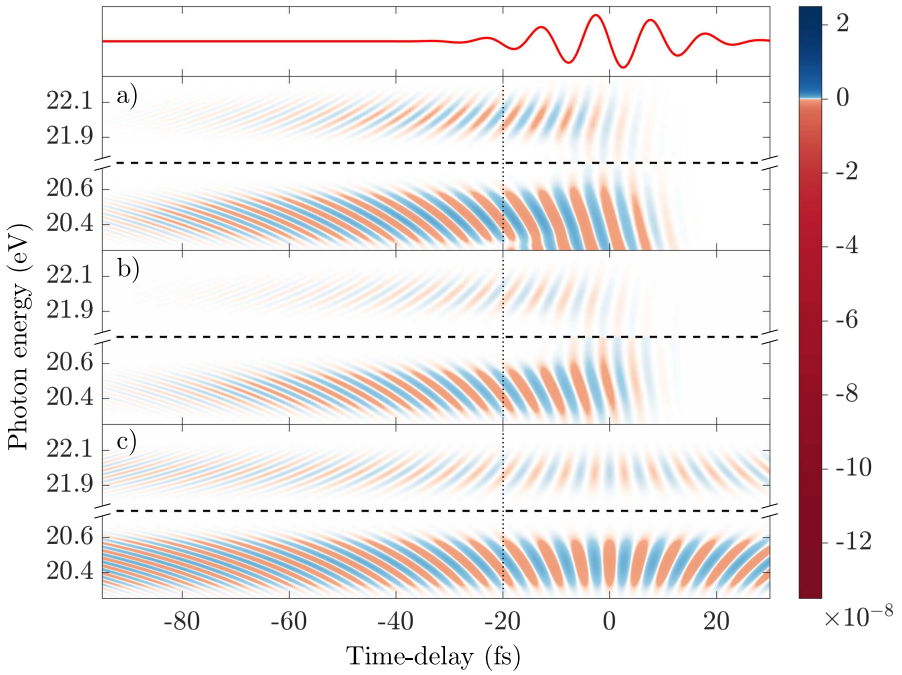

Figure 3.3: Attosecond transient absorption spectra $\tilde{S}(\omega,\tau)$ [Eq. (2.1)] focused on the rapidly oscillating fringes around the energies $E(1s2p) \pm 2\omega_{\mathrm{IR}}$ in He. In (a) $\tilde{d}(\omega,\tau)$ is determined via the time-dependent Schrödinger equation [see Eq. (2.6)] with a basis of $N+1=3$ levels, as in Fig. 2.1 (b). In (b) $\tilde{d}(\omega,\tau)$ is calculated from the adiabatic three-level model, with the LIS seen in (a) (between -25 fs $< \tau <$ 15 fs, centered at $E = 20.23$ eV) removed by keeping only the first term of Eq. (2.24); resulting in an unobstructed view of the fringes. In (c) the analytic solution from Eq. (2.32) is shown. The vertical dotted line serves as a guide for the eye. The top panel illustrates the infrared pulse centered at $\tau = 0$ fs. The color scale to the right shows the signal strength in arbitrary units. For pulse parameters see text following Eq. (2.2).

analytic solution from Eq. (2.34) is shown in Fig. 3.4 (c), and it exhibits qualitative and quantitative agreement with the full numerical solution from Fig. 3.4 (b). The discrepancy beyond relatively small positive delays does not undermine the main result; as discussed for the SBs and fringes above.

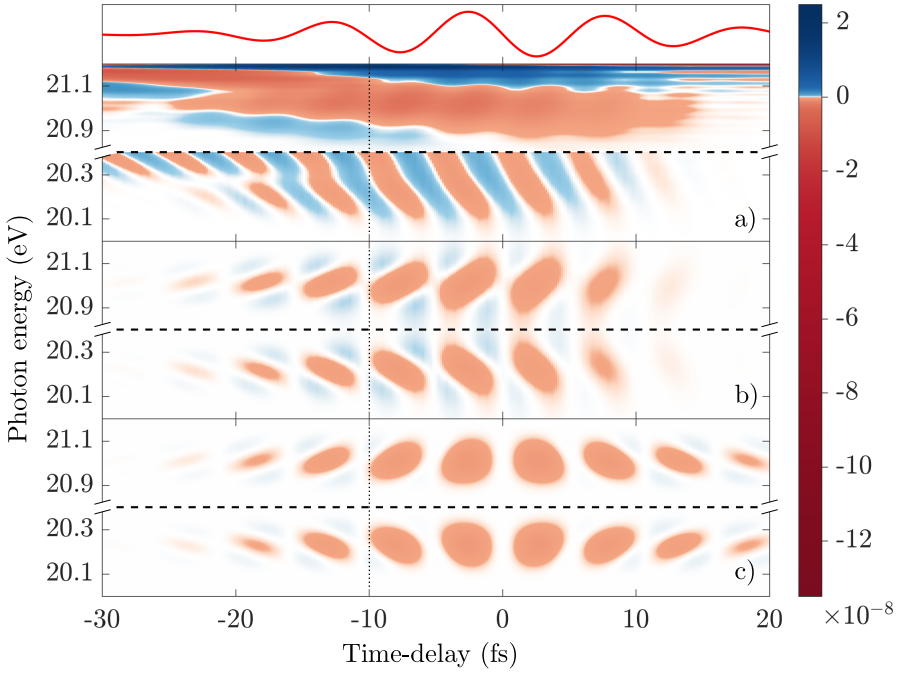

Figure 3.4: Attosecond transient absorption spectra $\tilde{S}(\omega, \tau)$ [Eq. (2.1)] focused on the light-induced structures (LISs) around the energies $E(1s2s) \pm \omega_{\mathrm{IR}}$ in He. In (a) $\tilde{d}(\omega, \tau)$ is determined via the time-dependent Schrödinger equation [see Eq. (2.6)] with a basis of $N + 1 = 3$ levels, as in Fig. 2.1 (b). In (b) $\tilde{d}(\omega, \tau)$ is calculated from the adiabatic three-level model, with the hyperbolic sidebands and oscillating fringes seen in (a) removed by keeping only the second term of Eq. (2.24); resulting in an unobstructed view of the LISs. (c) shows the analytic solution from Eq. (2.34). The vertical dotted line serves as a guide for the eye. The top panel illustrates the infrared pulse centered at $\tau = 0$ fs. The color scale to the right shows the signal strength in arbitrary units. For pulse parameters see text following Eq. (2.2).

Chapter 4

Summary and Outlook

In this progress report we have detailed the derivation of closed analytical expressions describing three features commonly encountered in ATAS: Fringes, SBs and LISs [Eqs. (2.32) and (2.34)]. The starting ansatz of this derivation was a three-level model subject to an adiabatic condition, where the excited states were instantaneous eigenvectors of a reduced Hamiltonian, which was followed by a series of approximations, ultimately leading to the analytic forms. We used as a reference for comparison a method in which the TDSE was solved numerically, and showed that the numerical solutions remained unaffected in the relevant energy range as additional states were added to the calculations. The three-level TDSE-based solution was compared with the full adiabatic model with agreeable qualitative and quantitative results, but with certain discrepancies due to the approximative methods implemented. Finally the process of going from a general TDSE reference solution to analytic expressions was examined for each of the three features separately. The SBs and the oscillating fringes were well described by the analytic expression when compared to the numerical methods. Moreover, the results [Eq. (2.32)] indicate a unification of these two features, which previously have been attributed to distinct processes; specifically perturbed free-induction decay [13, 14] and optical quantum interference [11]. Important characteristics of the LISs were correctly reproduced by the analytical expression. The derivation and the final form of the closed analytical expressions revealed the origin of the considered features. The expressions directly showed how the fringes, SBs and LISs depend on the properties of the pulses, such as their field strengths and the IR frequency and duration; as well as the dependence of the features on system specific parameters, i.e. energies and transition dipole moments. We can therefore expect that they can be used to analyze experimental and numerical ATAS spectra, and to identify uniquely these types of features in the spectra; for example by comparing the scaling in intensity of certain features in a spectrum with that predicted analytically. Given the current experimental capabilities with respect to wavelengths and intensities, we expect that validity conditions for the model can be fulfilled in many different atomic systems.

The method of ATAS has since 2010 seen comprehensive use on various atomic systems, as mentioned in the introduction. Theoretical treatments have been applied

that describe most of the features found in spectra obtained through this method. Studies on molecular systems, however, imply additional degrees of complexity relative to atomic systems. Consequently, molecules have not yet been subjected to the same scrutiny. Some studies have been performed however; notably experimental investigations on the nitrogen molecule by Warrick et al [24, 25] and theoretical modeling by Bækhøj et al [21, 26, 27] on the hydrogen molecule. The plan for the rest of the present Ph.D. project involves a numerical study of the lithium fluoride molecule, for which potential energy curves and dipole moments are available [28]. We hope to gain an increased understanding of the molecular processes appearing in the context of ATAS. After this we will also consider the possibility for conducting analytic modeling of the features in the molecular spectra, akin to the work reported herein.

As part of my Ph.D. program, a brief stay at Louisiana State University in the United States is planned.

Appendix A

Fourier transform of $\langle \mathbf{d(t)} \rangle_\mathbf{1}$ and $\langle \mathbf{d(t)} \rangle_\mathbf{2}$

In this Appendix we show how to obtain the Fourier transform of the time-dependent dipole moment corresponding to the SBs, fringes and LISs in the ATA spectrum, described by Eq. (2.31).

Following the convention

$$\mathcal{F}[f(t)](\omega) = \frac{1}{\sqrt{2\pi}} \int_{-\infty}^{\infty} dt f(t) e^{-i\omega t}, \tag{A.1}$$

and starting with the dipole moment corresponding to the SBs and fringes, we wish to solve

$$\tilde{d}_1(\omega, \tau) = \frac{\alpha d_{01}^2 d_{12}^2}{\sqrt{2\pi}(E_1 - E_2)} e^{-iE_1\tau} \int_{-\infty}^{\infty} dt\, e^{iE_1 t} e^{-i\omega t} \left[\int_{\tau}^{t} dt' \mathcal{E}_{\mathrm{IR}}^2(t') + \frac{i\mathcal{E}_{\mathrm{IR}}^2(t)}{2(E_1 - E_2)} \right]. \tag{A.2}$$

The factor $e^{iE_1 t}$ will only cause a shift in frequency, which can be taken into consideration afterwards. The field $\mathcal{E}_{\mathrm{IR}}(t)$ is obtained from Eq. (2.2):

$$\mathcal{E}_{\mathrm{IR}}(t) = \frac{A_{0,\mathrm{IR}} 8t}{T_{\mathrm{IR}}^2} e^{-\frac{4t^2}{T_{\mathrm{IR}}^2}} \cos(\omega_{\mathrm{IR}} t) + \mathcal{E}_{0,\mathrm{IR}} e^{-\frac{4t^2}{T_{\mathrm{IR}}^2}} \sin(\omega_{\mathrm{IR}} t), \tag{A.3}$$

where we have set $t_c = 0$. The IR field in our calculations has a relatively large period T_{IR}, suggesting that we can neglect the term with the factor T_{IR}^{-2}. The remaining term consist of an envelope part (the exponential factor) and a carrier part (the sine factor).

Starting with the first of the two terms in Eq. (A.2), the integral can be split up as

$$\int_{\tau}^{t} dt' \mathcal{E}_{\mathrm{IR}}^2(t') = \int_{0}^{t} dt' \mathcal{E}_{\mathrm{IR}}^2(t') + \int_{\tau}^{0} dt\, \mathcal{E}_{\mathrm{IR}}^2(t), \tag{A.4}$$

where the second integral will be constant in time after evaluation and can be dropped, following the arguments leading up to Eq. (2.31). Noting that the integrand is even, we

may rewrite the expression further

$$\begin{aligned}\int_0^t dt' \mathcal{E}_{\mathrm{IR}}^2(t') =& \frac{1}{2}\int_{-t}^{t} dt' \mathcal{E}_{\mathrm{IR}}^2(t') \\ =& \frac{1}{2}\left[\int_{-\infty}^{-t} dt' \mathcal{E}_{\mathrm{IR}}^2(t') + \int_{-t}^{t} dt' \mathcal{E}_{\mathrm{IR}}^2(t') - \int_{t}^{\infty} dt' \mathcal{E}_{\mathrm{IR}}^2(t')\right] \\ =& \frac{1}{2}\int_{-\infty}^{\infty} dt' \mathrm{sgn}(t-t') \mathcal{E}_{\mathrm{IR}}^2(t'),\end{aligned} \tag{A.5}$$

where $\mathrm{sgn}(t)$ is the sign function. The final expression in Eq. (A.5) can be recognized as the convolution of the functions $\mathrm{sgn}(t'-t) \equiv f(t')$ and $\mathcal{E}_{\mathrm{IR}}^2(t') \equiv g(t')$, defined as

$$(f * g)(t) \equiv \int_{-\infty}^{\infty} dt' f(t-t') g(t'). \tag{A.6}$$

From the convolution theorem we have

$$\mathcal{F}[(f*g)(t)](\omega) = \sqrt{2\pi}\mathcal{F}[f(t)](\omega)\mathcal{F}[g(t)](\omega), \tag{A.7}$$

reducing the problem to finding the individual Fourier transforms of $f(t)$ and $g(t)$. The former is given by [29]

$$\mathcal{F}[\mathrm{sgn}(t)](\omega) = \sqrt{\frac{2}{\pi}}\frac{1}{i\omega}. \tag{A.8}$$

The latter is more involved:

$$\mathcal{F}[\mathcal{E}_{\mathrm{IR}}^2(t)](\omega) = \frac{\mathcal{E}_{0,\mathrm{IR}}^2}{\sqrt{2\pi}}\int_{-\infty}^{\infty} dt \exp\left(-\frac{8t^2}{T_{\mathrm{IR}}^2}\right)\sin^2(\omega_{\mathrm{IR}} t) e^{-i\omega t}, \tag{A.9}$$

and can be solved by expressing the sine as exponentials and completing the square, resulting in

$$\begin{aligned}\mathcal{F}[\mathcal{E}_{\mathrm{IR}}^2(t)](\omega) =& -\frac{\mathcal{E}_{0,\mathrm{IR}}^2 T_{\mathrm{IR}}}{16}\Bigg[-2\exp\left(-\frac{T_{\mathrm{IR}}^2\omega^2}{32}\right) \\ &+ \exp\left(-\frac{T_{\mathrm{IR}}^2(\omega+2\omega_{\mathrm{IR}})^2}{32}\right) + \exp\left(-\frac{T_{\mathrm{IR}}^2(\omega-2\omega_{\mathrm{IR}})^2}{32}\right)\Bigg],\end{aligned} \tag{A.10}$$

which also solves the Fourier transform of the second term in Eq. (A.2).

From Eqs. (A.2), (A.5), (A.7), (A.8) and (A.10), and by incorporating the shift in frequency due to the factor $e^{iE_1 t}$, we obtain

$$\begin{aligned}\tilde{d}_1(\omega,\tau) =& \frac{i\alpha d_{01}^2 d_{12}^2 \mathcal{E}_{0,\mathrm{IR}}^2 T_{\mathrm{IR}}}{16(E_1-E_2)} e^{-iE_1\tau}\left[\frac{1}{\omega-E_1} - \frac{1}{2(E_1-E_2)}\right] \\ &\times\Bigg\{\exp\left[\frac{-T_{\mathrm{IR}}^2(\omega-E_1-2\omega_{\mathrm{IR}})^2}{32}\right] + \exp\left[\frac{-T_{\mathrm{IR}}^2(\omega-E_1+2\omega_{\mathrm{IR}})^2}{32}\right] \\ &- 2\exp\left[\frac{-T_{\mathrm{IR}}^2(\omega-E_1)^2}{32}\right]\Bigg\}.\end{aligned} \tag{A.11}$$

Next, to obtain the Fourier transform of the time-dependent dipole moment corresponding to LISs, we start with the Fourier transform of Eq. (2.33):

$$\tilde{d}_2(\omega,\tau) = -\frac{i\alpha d_{01}^2 d_{12}^2}{\sqrt{2\pi}(E_1-E_2)^2}\mathcal{E}_{\mathrm{IR}}(\tau)e^{-iE_2\tau} \times \int_{-\infty}^{\infty} dt\, e^{iE_2 t}\mathcal{E}_{\mathrm{IR}}(t)e^{-i\omega t}, \tag{A.12}$$

and we make the same approximation for the IR field as above. Solving the integral then amounts to taking the Fourier transform of a Gaussian and performing shifts $E_2 \pm \omega_{\mathrm{IR}}$ in frequency. Thus, the Fourier transformed dipole moment responsible for the LISs is

$$\begin{aligned}\tilde{d}_2(\omega,\tau) = &-\frac{\alpha d_{01}^2 d_{12}^2 \mathcal{E}_{0,\mathrm{IR}}^2 T_{\mathrm{IR}}}{4\sqrt{2\pi}(E_1-E_2)^2}\exp\left(-iE_2\tau\right)\exp\left[\frac{-4\tau^2}{T_{\mathrm{IR}}^2}\right]\sin\left(\omega_{\mathrm{IR}}\tau\right) \\ &\times\left\{\exp\left[-\frac{T_{\mathrm{IR}}^2(\omega-E_2-\omega_{\mathrm{IR}})^2}{16}\right]-\exp\left[-\frac{T_{\mathrm{IR}}^2(\omega-E_2+\omega_{\mathrm{IR}})^2}{16}\right]\right\}.\end{aligned} \tag{A.13}$$

Bibliography

[1] J. J. Rørstad, J. E. Bækhøj, and L. B. Madsen. Analytic modeling of structures in attosecond transient-absorption spectra. *ArXiv e-prints*, April 2017.

[2] F. Krausz and M. Ivanov. Attosecond physics. *Rev. Mod. Phys.*, 81:163–234, Feb 2009.

[3] M. Hentschel, R. Kienberger, Ch. Spielmann, G. A. Reider, N. Milosevic, T. Brabec, P. Corkum, U. Heinzmann, M. Drescher, and F. Krausz. Attosecond metrology. *Nature*, 414(6863):509–513, 2001.

[4] K. Zhao, Q. Zhang, M. Chini, Y. Wu, X. Wang, and Z. Chang. Tailoring a 67 attosecond pulse through advantageous phase-mismatch. *Optics letters*, 37(18):3891–3893, 2012.

[5] A. L'Huillier and Ph. Balcou. High-order harmonic generation in rare gases with a 1-ps 1053-nm laser. *Physical Review Letters*, 70(6):774, 1993.

[6] M. Lewenstein, Ph. Balcou, M. Y. Ivanov, A. L'Huillier, and P. B. Corkum. Theory of high-harmonic generation by low-frequency laser fields. *Physical Review A*, 49(3):2117, 1994.

[7] E. Goulielmakis, Z.-H. Loh, A. Wirth, R. Santra, N. Rohringer, V. S. Yakovlev, S. Zherebtsov, T. Pfeifer, A. M. Azzeer, M. F. Kling, et al. Real-time observation of valence electron motion. *Nature*, 466(7307):739–743, 2010.

[8] H. Wang, M. Chini, S. Chen, C.-H. Zhang, F. He, Y. Cheng, Y. Wu, U. Thumm, and Z. Chang. Attosecond time-resolved autoionization of argon. *Phys. Rev. Lett.*, 105:143002, Oct 2010.

[9] A. Kaldun, A. Blättermann, V. Stooß, S. Donsa, H. Wei, R. Pazourek, S. Nagele, C. Ott, C.D. Lin, J. Burgdörfer, et al. Observing the ultrafast buildup of a fano resonance in the time domain. *Science*, 354(6313):738–741, 2016.

[10] S. Chen, M. Wu, M. B. Gaarde, and K. J. Schafer. Quantum interference in attosecond transient absorption of laser-dressed helium atoms. *Phys. Rev. A*, 87:033408, Mar 2013.

[11] M. Chini, X. Wang, Y. Cheng, and Z. Chang. Resonance effects and quantum beats in attosecond transient absorption of helium. *Journal of Physics B: Atomic, Molecular and Optical Physics*, 47(12):124009, 2014.

[12] S. Chen, M. J. Bell, A. R. Beck, H. Mashiko, M. Wu, A. N. Pfeiffer, M. B. Gaarde, D. M. Neumark, S. R. Leone, and K. J. Schafer. Light-induced states in attosecond transient absorption spectra of laser-dressed helium. *Phys. Rev. A*, 86:063408, Dec 2012.

[13] M. Lindberg and S. W. Koch. Transient oscillations and dynamic stark effect in semiconductors. *Phys. Rev. B*, 38:7607–7614, Oct 1988.

[14] C. H. Brito Cruz, J. P. Gordon, P. C. Becker, R. L. Fork, and C. V. Shank. Dynamics of spectral hole burning. *IEEE Journal of Quantum Electronics*, 24(2):261–269, Feb 1988.

[15] S. H. Autler and C. H. Townes. Stark effect in rapidly varying fields. *Phys. Rev.*, 100:703–722, Oct 1955.

[16] A. N. Pfeiffer and S. R. Leone. Transmission of an isolated attosecond pulse in a strong-field dressed atom. *Phys. Rev. A*, 85:053422, May 2012.

[17] M. Wu, S. Chen, M. B. Gaarde, and K. J. Schafer. Time-domain perspective on autler-townes splitting in attosecond transient absorption of laser-dressed helium atoms. *Phys. Rev. A*, 88:043416, Oct 2013.

[18] W. Dong, Y. Li, X. Wang, J. Yuan, and Z. Zhao. Analysis of interference in attosecond transient absorption in adiabatic condition. *Phys. Rev. A*, 92:033412, Sep 2015.

[19] M. B. Gaarde, C. Buth, J. L. Tate, and K. J. Schafer. Transient absorption and reshaping of ultrafast xuv light by laser-dressed helium. *Phys. Rev. A*, 83:013419, Jan 2011.

[20] J. C. Baggesen, E. Lindroth, and L. B. Madsen. Theory of attosecond absorption spectroscopy in krypton. *Phys. Rev. A*, 85:013415, Jan 2012.

[21] J. E. Bækhøj, L. Yue, and L. B. Madsen. Nuclear-motion effects in attosecond transient-absorption spectroscopy of molecules. *Phys. Rev. A*, 91:043408, Apr 2015.

[22] G. W. F. Drake. *Handbook of Atomic, Molecular, and Optical Physics*. Springer, New York, 2006.

[23] M. Wu, S. Chen, S. Camp, K. J. Schafer, and M. B. Gaarde. Theory of strong-field attosecond transient absorption. *Journal of Physics B: Atomic, Molecular and Optical Physics*, 49(6):062003, 2016.

[24] E. R. Warrick, W. Cao, D. M. Neumark, and S. R. Leone. Probing the dynamics of rydberg and valence states of molecular nitrogen with attosecond transient absorption spectroscopy. *The Journal of Physical Chemistry A*, 120(19):3165–3174, 2016. PMID: 26862883, http://dx.doi.org/10.1021/acs.jpca.5b11570.

[25] Erika R. Warrick, Jens E. Bækhøj, Wei Cao, Ashley P. Fidler, Frank Jensen, Lars Bojer Madsen, Stephen R. Leone, and Daniel M. Neumark. Attosecond transient absorption spectroscopy of molecular nitrogen: Vibrational coherences in the $b'\ ^1\sum_u^+$ state. *Chemical Physics Letters* (2017), http://dx.doi.org/10.1016/j.cplett.2017.02.013.

[26] J. E. Bækhøj and L. B. Madsen. Light-induced structures in attosecond transient-absorption spectroscopy of molecules. *Phys. Rev. A*, 92:023407, Aug 2015.

[27] J. E. Bækhøj and L. B. Madsen. Attosecond transient-absorption spectroscopy on aligned molecules. *Phys. Rev. A*, 94:043414, Oct 2016.

[28] H.-J. Werner and W. Meyer. MCSCF study of the avoided curve crossing of the two lowest $^1\sum^+$ states of LiF. *The Journal of Chemical Physics*, 74(10):5802–5807, 1981.

[29] D. W. Kammler. *A first course in Fourier analysis*. Cambridge University Press, Cambridge, 2007.